Dalton Transactions

ROYAL SOCIETY OF CHEMISTRY

PAPER

View Article Online
View Journal | View Issue

Cite this: *Dalton Trans.*, 2025, **54**, 8152

Design of a high-performance infrared birefringent crystal $Ba_4HgP_2Se_{10}$ *via* a low-dimensional motif intercalation strategy†

Zhihui Xiong,[a] Haotian Tian,*[b] Zhixi Li,[a] Guowei Deng,*[a] Fang Ding,[a] Qian Wu[b] and Mingjun Xia*[b]

Received 23rd January 2025,
Accepted 8th April 2025

DOI: 10.1039/d5dt00186b

rsc.li/dalton

The development of birefringent materials, especially infrared (IR) birefringent crystals, has been limited by conflicting microstructural requirements, such as broad transmission range, wide band gap, and large birefringence. In this work, we propose a "low-dimensional motif intercalation" strategy for designing high-performance birefringent materials. Utilizing the layered selenophosphorus $Ba_3P_2Se_8$ as a prototype compound, a novel IR birefringent crystal $Ba_4HgP_2Se_{10}$ with enhanced birefringence was successfully synthesized by the intercalation of the linear $[HgSe_2]^{2-}$ moieties, while the outstanding optical properties such as wide band gap and long IR cutoff were maintained. Notably, the $Ba_4HgP_2Se_{10}$ crystal exhibits the largest band gap among known selenophosphorus compounds, accompanied by a wide IR transmittance range and substantial birefringence. Theoretical calculations reveal that the outstanding optical properties of $Ba_4HgP_2Se_{10}$ arise from the synergistic interaction between Ba^{2+} cations, $[HgSe_2]^{2-}$ anions, and the layered selenophosphorus framework.

Introduction

Birefringent crystals, which can modulate the polarization states of light, play an important role in laser technology and optoelectronics including polarizers, isolators, and phase retarders.[1–7] Current commercial birefringent crystals can meet the application demands in the short-wave ultraviolet (UV), visible, and near-infrared (IR) regions. However, birefringent crystals suitable for the IR region remain scarce. In recent years, the rapid advancement of IR laser technology has heightened the demand for IR birefringent crystals.[8] Generally, a qualified IR birefringent crystal must not only exhibit high birefringence but also have a large band gap and a wide IR transmission range.[8–10] Unfortunately, these properties impose conflicting requirements on the microstructure, making it challenging to design them simultaneously in a single crystal.

Traditional birefringent crystals are primarily composed of halides and oxides. Among them, oxide crystals have long been the focus of research due to their excellent birefringence and large band gaps. Many outstanding oxide birefringent crystals, such as YVO_4,[11] $LiNbO_3$,[12] $CaCO_3$,[13] TiO_2,[14] and α-BaB_2O_4,[15] have been developed over the years. However, the absorption vibrations of metal–oxygen bonds in these oxide crystals severely limit their IR transmission range, not suitable for IR wavelength range applications. In contrast, the halide crystal MgF_2 not only has a large band gap but also exhibits high transparency from the UV to IR region. Unfortunately, its practical application is significantly restricted by its weak birefringence (0.012@1064 nm).[16] Therefore, there is a pressing need to develop birefringent crystals for IR applications. Sulfides, phosphides, and selenides have long been studied as classical candidates for IR optoelectronic materials. Among these, selenides typically exhibit a wider IR transmission range than phosphides and sulphides, as the heavier atomic mass of selenium can effectively reduce lattice vibrational phonon energy.[17] In recent years, several excellent selenide IR crystals have been developed, such as $BaGa_4Se_7$,[18] $PbGa_4Se_7$,[19] $BaGa_2GeSe_6$,[20] $NaAsSe_2$,[21] $BaHgGeSe_4$,[22] and $PbGa_2GeSe_6$.[23] However, due to the selenium's relatively weak electronegativity, the most reported selenide crystals have a smaller band gap with a low laser damage threshold, making them

[a]*School of Innovation and Entrepreneurship, Chengdu Normal University, Chengdu 611130, China. E-mail: guoweideng86@163.com*

[b]*Beijing Center for Crystal Research and Development, Key Laboratory of Functional Crystals and Laser Technology, Technical Institute of Physics and Chemistry, Chinese Academy of Sciences, Beijing 100190, China. E-mail: tianhaotian@mail.ipc.ac.cn, xiamingjun@mail.ipc.ac.cn*

†Electronic supplementary information (ESI) available: Crystallographic data and structural data (Tables S1–S4), figures presenting the calculation results of $Ba_3P_2Se_8$ (Fig. S1), and figures presenting the measurement results and details of $Ba_4HgP_2Se_{10}$ (Fig. S2–S8). CCDC 2413877 for $Ba_4HgP_2Se_{10}$. For ESI and crystallographic data in CIF or other electronic format see DOI: **https://doi.org/10.1039/d5dt00186b**

susceptible to photorefractive damage. Therefore, the exploration of an effective strategy to balance the three key properties —wide transmission range, high birefringence, and large band gap—is critical for the design of high-performance IR birefringent crystals.

According to the functional motif theory, the macroscopic optical properties of crystals are closely related to the microscopic optical properties of the constituted functional motifs and their arrangements.[24] In general, low-dimensional functional motifs, such as two-dimensional (2D) planar groups and one-dimensional (1D) linear units, typically exhibit high polarizability anisotropy, which promotes the formation of large birefringence.[25] Additionally, heavy elements can effectively lower the phonon energy of lattice vibrations, thereby extending the IR transmission range. Functional motifs with a strong covalent character typically exhibit a large HOMO–LUMO gap, which contributes to broadening the band gap.[26–31] A crystal that incorporates all these characteristics can achieve a balance between IR transmission, birefringence, and band gap. In principle, these features can be simultaneously realized by integrating functional motifs into a suitable and easily modifiable structural framework.

In this work, we propose a "low-dimensional motif intercalation" strategy, which involves constructing a multifunctional 2D layered framework suitable for the IR region and introducing low-dimensional functional motifs between its layers. This is mainly based on the following three considerations: (i) the balance between the band gap and the IR cutoff can be achieved by selecting appropriate building blocks for the layered framework; (ii) the weaker binding energy between adjacent layers provides significant flexibility for introducing additional functional units with high polarizability anisotropy, offering a unique opportunity to enhance birefringence; and (iii) the layered framework itself exhibits relatively high anisotropy, which also contributes to the birefringence. To implement this strategy, we focused on selenophosphorus for the selection of the layered framework construction templates. On the one hand, the heavier atomic mass of selenium contributes to a broader IR transmission range in crystals. On the other hand, the similarity in electronegativity between phosphorus and selenium enables the formation of relatively strong covalent bonds, contributing to the expansion of the band gap. Furthermore, considering that the introduction of alkaline earth metal elements can effectively reduce the dispersion of the compounds, the Ba^{2+} ion was selected as a counter ion to further increase the atomic mass. Based on these considerations, a selenophosphorus compound $Ba_3P_2Se_8$ with a layered structure was screened as a prototype compound, as expected, which can achieve a balance between a large band gap and a long IR cutoff (Fig. S1†). To further enhance its birefringence (theoretical calculations show that its birefringence is 0.095@1064 nm), guided by the above design strategy, the linear $[HgSe_2]^{2-}$ unit was further introduced into the interlayer, while hoping that its heavier mass can further extend the IR transmission range. Accordingly, a novel birefringent crystal $Ba_4HgP_2Se_{10}$ was successfully synthesized. Notably, the synergy between the selenophosphorus layered framework and $[HgSe_2]^{2-}$ units resulted in a broad IR transmission range, a large birefringence (0.152@1064 nm), and a wide band gap (2.45 eV), achieving an optimal balance among the three key performance parameters. In particular, the band gap of $Ba_4HgP_2Se_{10}$ was the widest observed among selenophosphides to date. Herein, we report its synthesis, crystal structure, optical properties, and theoretical calculations.

Experimental section

Reagents

P (Alfa Aesar, 99.9%), Se (Alfa Aesar, 99.99%), HgSe (Alfa Aesar, 99.99%), and BaSe (Alfa Aesar, 99.7%).

Synthesis

Powder samples of $Ba_4HgP_2Se_{10}$ were synthesized using a high-temperature solid-phase method. The reaction mixture, consisting of 1 mmol HgSe, 4 mmol BaSe, 2 mmol P, and 5 mmol Se, was ground and sealed in a quartz tube, and then heated to 600 °C. After 10 hours, the mixture was cooled to room temperature, resulting in the formation of pure-phase $Ba_4HgP_2Se_{10}$ powder. Single crystal samples of $Ba_4HgP_2Se_{10}$ were obtained by a similar method. A mixture of 1 mmol HgSe, 4 mmol BaSe, 1.5 mmol P, and 6 mmol Se was prepared, ground, and sealed in a quartz tube. The tube was then heated to 900 °C to induce melting. After 3 days, the mixture was slowly cooled to room temperature at a rate of 4 °C h^{-1}, resulting in the formation of $Ba_4HgP_2Se_{10}$ crystals.

Power X-ray diffraction (PXRD)

The PXRD data of $Ba_4HgP_2Se_{10}$ were recorded on a Bruker D8 powder X-ray diffractometer with Cu Kα radiation (λ = 1.5418 Å) in the 2θ range from 10 to 70°.

Energy-dispersive X-ray spectroscopy analysis

Microprobe elemental analyses were conducted on a field emission scanning electron microscope (FESEM, SU-8010) with an energy-dispersive X-ray spectroscope (EDS).

Single-crystal X-ray diffraction

Single-crystal X-ray diffraction data were collected using a Rigaku XtaLAB Synergy diffractometer, equipped with graphite-monochromated Mo-Kα radiation (λ = 0.71073 Å). The crystal structure of $Ba_4HgP_2Se_{10}$ was solved using ShelXT and refined using ShelXL, both within the OLEX2 software package.[32] Crystallographic data and structure refinements for $Ba_4HgP_2Se_{10}$ are provided in Table S1.† Atomic coordinates, equivalent isotropic displacement parameters, and selected bond lengths and angles, as well as anisotropic displacement parameters, are presented in Tables S2–S4.†

Thermal analysis

The thermal properties of $Ba_4HgP_2Se_{10}$ samples were investigated using a Labsys TG-DTA1600 simultaneous thermal analyzer under vacuum at a heating/cooling rate of 20 °C min^{-1}.

UV-Vis diffuse reflectance spectroscopy

The diffuse reflectance spectrum of $Ba_4HgP_2Se_{10}$ was recorded on a Cary 7000 UV-vis-NIR spectrophotometer. Polytetrafluoroethylene (PTFE) was used as a 100% reflectance standard.

Infrared spectroscopy

Infrared (IR) spectra were recorded using a Bruker VERTEX 70 Fourier IR spectrometer in the range of 400–3000 cm^{-1}. Polycrystalline samples and KBr were ground and pressed into transparent pellets for the measurement.

Theoretical calculations

The band structures of $Ba_4HgP_2Se_{10}$ and $Ba_3P_2Se_8$ were calculated using the CASTEP package based on density functional theory (DFT).[33] The exchange-correlation energy was treated with the generalized gradient approximation (GGA) using the Perdew–Burke–Ernzerhof (PBE) functional.[34] The following orbital electrons were considered as valence electrons: Ba $5s^2$ $5p^6$ $6s^2$; Hg $5d^{10}$ $6s^2$; P, $3s^2$ $3p^3$; and Se $4s^2$ $4p^4$. The energy cutoffs for $Ba_4HgP_2Se_{10}$ and $Ba_3P_2Se_8$ were set to 400 eV and 350 eV, respectively. The Monkhorst–Pack grid sizes for $Ba_4HgP_2Se_{10}$ and $Ba_3P_2Se_8$ were $2 \times 1 \times 1$ and $1 \times 2 \times 1$, respectively.[35] The polarizability anisotropy values of the [$HgSe_2$] and [PSe_4] units were calculated using the B3LYP/def2-TZVP method.

Results and discussion

Yellow colored $Ba_4HgP_2Se_{10}$ crystals were prepared using a high-temperature method. The obtained crystals can remain stable in air for several months. The powder XRD pattern aligns closely with the spectrum derived from the crystal structure, confirming that the as-synthesized samples are of pure phase (Fig. S2†). EDS confirmed that the crystals were composed of Ba, Hg, P, and Se elements (Fig. S3†). Thermal analysis indicates that the $Ba_4HgP_2Se_{10}$ crystals are stable up to 531 °C, demonstrating excellent thermal stability (Fig. S4†).

$Ba_3P_2Se_8$ crystallizes in the centrosymmetric space group $P2_1/a$ of the monoclinic crystal system. The structure features two distinct environments for P atoms (P1 and P2) and two environments for Ba ions (Ba1 and Ba2). Both P1 and P2 atoms coordinate with four Se atoms to form [PSe_4] tetrahedra, with P–Se bond lengths ranging from 2.208 to 2.220 Å. Two [PSe_4] tetrahedra extend along the *a*- and *b*-axes through the connection of Ba1 ions, forming two nearly opposite polar layers (Fig. 1a and b). These polar layers are interconnected *via* Ba1 ions to create a double-layer framework (Fig. 1a). This framework is further stabilized along the *c*-axis by Ba2 cations, ultimately resulting in the three-dimensional (3D) crystal structure of $Ba_3P_2Se_8$ (Fig. 1b).

$Ba_4HgP_2Se_{10}$ crystallizes in the centrosymmetric space group $P\bar{1}$ of the triclinic crystal system. In the structure, there are nine crystallographically independent atoms with one Hg atom, two Ba atoms (Ba1 and Ba2), five Se atoms, and one P atom. Each P atom is coordinated to four Se atoms, forming a [PSe_4] tetrahedron with P–Se bond lengths ranging from 2.208 to 2.220 Å. Each Hg atom, in turn, is bonded to two Se atoms, forming a linear [$HgSe_2$] unit with an Hg–Se bond length of 2.440 Å. Due to the symmetry restrictions of the space group $P\bar{1}$, the [PSe_4] tetrahedra adopt two opposite orientations within the structure (Fig. 1c and d). Similarly to its parent compound $Ba_3P_2Se_8$, the two [PSe_4] tetrahedra in $Ba_4HgP_2Se_{10}$ extend along the *a*- and *b*-axes through the connection of Ba1 ions, thereby forming two oppositely oriented polar layers (Fig. 1c and d). The introduction of the [$HgSe_2$] units leads to the isolation of the two oppositely oriented [PSe_4] units, effectively inserting a non-polar layer composed of [$HgSe_2$] units and Ba1 ions between the two polar layers of $Ba_3P_2Se_8$. These three layers are interconnected *via* Ba1 ions, forming a non-polar three-layer structural framework (Fig. 1c and d). This framework is further extended along the *c*-axis by Ba2 ions, resulting in the formation of the 3D crystal structure of $Ba_4HgP_2Se_{10}$ (Fig. 1d).

As shown in Fig. 2a, the diffuse reflectance spectrum reveals a band gap of 2.45 eV for $Ba_4HgP_2Se_{10}$, corresponding to a cutoff wavelength of 506 nm. To the best of our knowledge, this is the widest band gap observed among selenophosphorus compounds, significantly greater than those of others including $K_2P_2Se_6$ (2.08 eV),[36] $Rb_2P_2Se_6$ (2.32 eV),[36] $KZrPSe_6$ (2.2 eV),[37] $RbZrPSe_6$ (2.2 eV),[37] $CsZrPSe_6$ (2.3 eV),[37] $KPSe_6$ (2.16 eV),[38,39] $RbPSe_6$ (2.18 eV),[38,39] $K_{0.6}Cs_{0.4}PSe_6$ (2.1 eV),[40] β-$CsPSe_6$ (1.9 eV),[40] KNb_2PSe_{10} (1.19 eV),[41] $RbNb_2PSe_{10}$ (1.16 eV),[41] $CsNb_2PSe_{10}$ (1.07 eV),[41] $Cs_5BiP_4Se_{12}$ (1.85 eV),[42] $Cs_5P_5Se_{12}$ (2.17 eV),[43] $K_4GeP_4Se_{12}$ (2.0 eV),[44] $Rb_4GeP_4Se_{12}$ (2.0 eV),[44] and $Cs_4GeP_4Se_{12}$ (2.0 eV).[44] To further understand the origin of this wide band gap, we calculated the band gap and PDOS curves of $Ba_4HgP_2Se_{10}$ and compared them with those of its parent compound, $Ba_3P_2Se_8$. As shown in Fig. S5,† $Ba_4HgP_2Se_{10}$ exhibits a higher calculated band gap compared to $Ba_3P_2Se_8$. Interestingly, the PDOS analysis shows that the top of the valence band and the bottom of the conduction band in both compounds are mainly composed of Se-p, P-s, P-p and Ba-d states, indicating that the band gap in both compounds is governed by the [PSe_4] unit and the ionic interactions between [PSe_4] units and Ba^{2+} ions (Fig. S6†). To further elucidate the microscopic mechanism underlying this band gap difference, we analyzed the electron density maps of the two compounds. As shown in Fig. S7,† the introduction of [$HgSe_2$] units in $Ba_4HgP_2Se_{10}$ effectively isolates the adjacent [PSe_4] tetrahedra, resulting in no overlap of the electron clouds between neighboring layers. It is likely that this structural difference inhibits electronic interactions between the adjacent [PSe_4] units, thus contributing to the widening of the band gap.

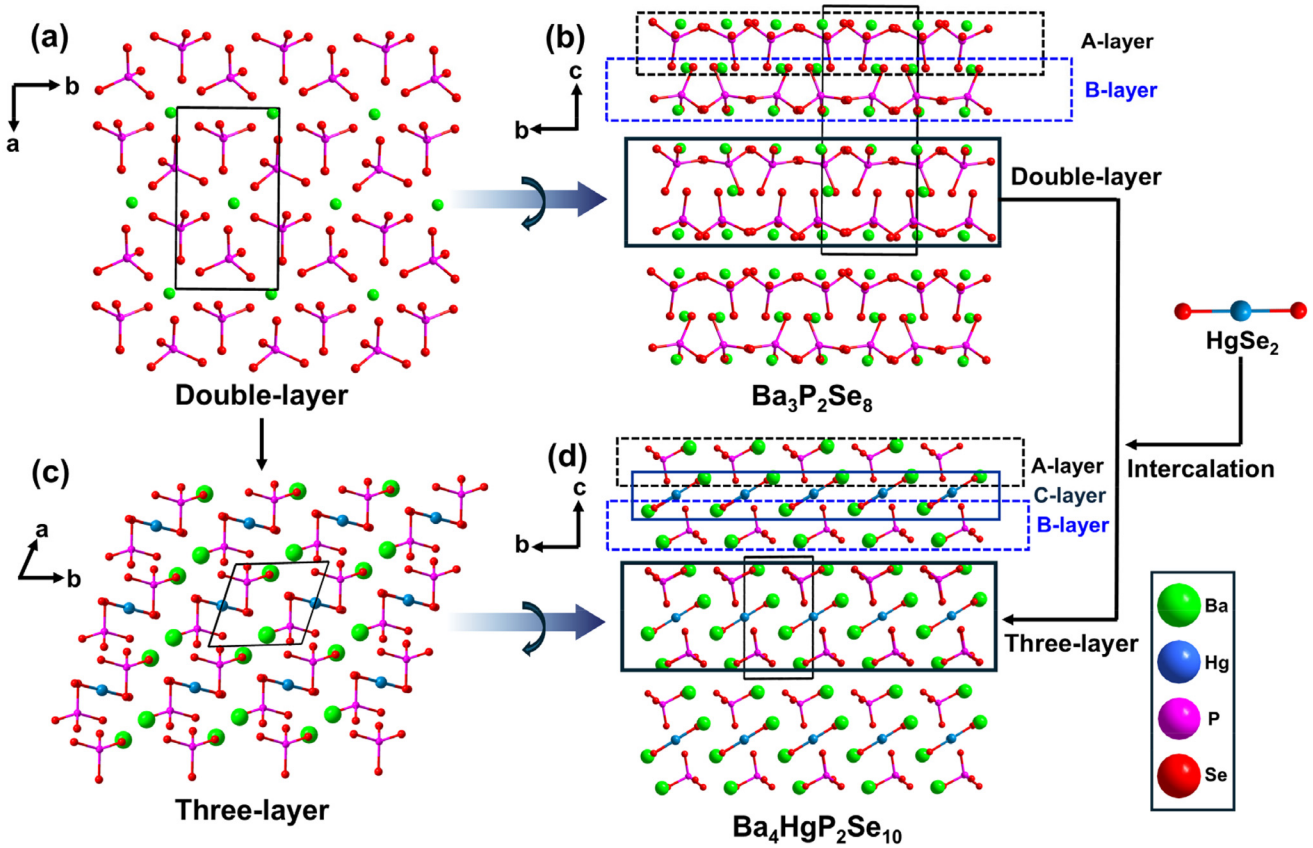

Fig. 1 (a) The double-layer of $Ba_3P_2Se_8$. (b) 3D crystal structure of $Ba_3P_2Se_8$ in the *bc* plane. (c) The three-layer of $Ba_4HgP_2Se_{10}$. (d) 3D crystal structure of $Ba_4HgP_2Se_{10}$ in the *bc* plane.

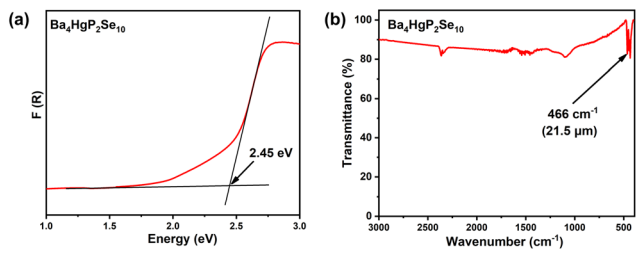

Fig. 2 (a) Measured optical band gap of $Ba_4HgP_2Se_{10}$. (b) IR transmittance spectrum of $Ba_4HgP_2Se_{10}$.

To characterize the transmission range of $Ba_4HgP_2Se_{10}$, IR spectra were measured. As shown in Fig. 2b, the IR cut-off edge of $Ba_4HgP_2Se_{10}$ is approximately 21.5 μm. Notably, this IR cut-off edge exceeds those of many well-known birefringent crystals, such as MgF_2 (7.04 μm),[16] $CaCO_3$ (2.3 μm),[13] YVO_4 (5 μm),[11] TiO_2 (4.5 μm),[14] $LiNbO_3$ (5 μm),[12] and α-BaB_2O_4 (3.5 μm).[15] It also outperforms several previously reported phosphide and sulfide crystals, including $CdSiP_2$ (9 μm),[45] $ZnGeP_2$ (12.5 μm),[46] $MgSiP_2$ (10.3 μm),[47,48] $AgGaS_2$ (13 μm),[49] and $AgGaSe_2$ (16 μm).[49] More importantly, such a long IR cut-off combined with a large band gap allows $Ba_4HgP_2Se_{10}$ to exhibit a wide transmission range superior to those of all commercial birefringent crystals to date (Fig. 4). Since the IR transmission range of materials is closely related to the phonon energy of lattice vibrations, we speculate that the exceptional IR transmission range of $Ba_4HgP_2Se_{10}$ is due to the relatively high atomic masses of Ba, Hg, P, and Se. These heavier atoms likely lower the phonon energy of lattice vibrations, thereby broadening the IR transmission range.

To characterize the birefringence of $Ba_4HgP_2Se_{10}$, refractive index dispersion curves were calculated. As shown in Fig. 3a, the refractive indices of $Ba_4HgP_2Se_{10}$ are $n[100] = 2.68$, $n[010] = 2.77$, and $n[001] = 2.62$ at a wavelength of 1064 nm, respectively, indicating that the birefringence of $Ba_4HgP_2Se_{10}$ at 1064 nm is 0.152 (Fig. 3b), significantly higher than that of its parent compound $Ba_3P_2Se_8$ (0.093 at 1064 nm). Notably, the experimental refractive indices of $Ba_4HgP_2Se_{10}$ will be obtained using the devices by cutting from the bulk crystal in the future. To elucidate the mechanism behind the enhancement of birefringence, the electron density maps of both compounds were calculated. As shown in Fig. S7,† although the electron density around the [PSe_4] unit is nearly isotropic, the laminar framework of $Ba_3P_2Se_8$ leads to significant interlayer voids that reduce the electron density along the *c*-axis. This results in a marked difference in the electron density between

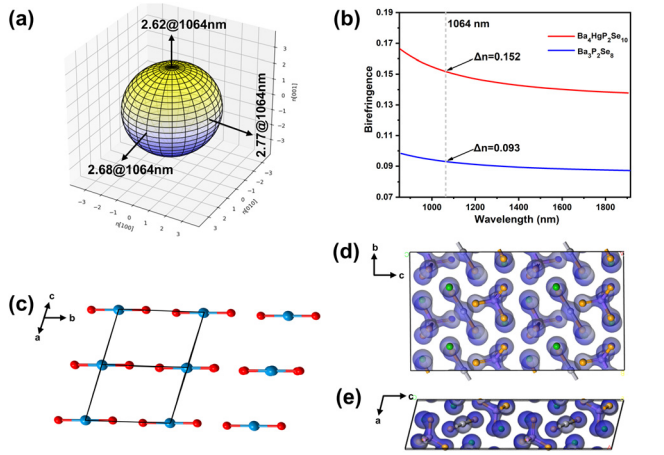

Fig. 3 (a) Triaxial ellipsoid of three refractive indices along the crystallographic axes of $Ba_4HgP_2Se_{10}$ at λ = 1064 nm. (b) Calculated birefringence of $Ba_4HgP_2Se_{10}$ and $Ba_3P_2Se_8$. (c) The arrangement of [$HgSe_2$] units in $Ba_4HgP_2Se_{10}$. (d) Calculated electron density in the *bc* plane for $Ba_4HgP_2Se_{10}$. (e) Calculated electron density in the *ac* plane for $Ba_4HgP_2Se_{10}$.

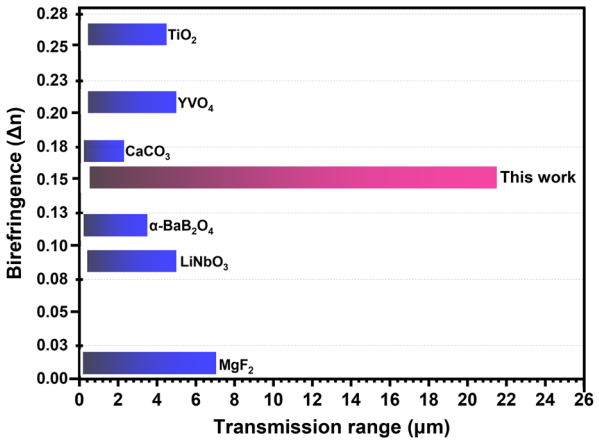

Fig. 4 Performance comparison chart of $Ba_4HgP_2Se_{10}$ with commercial birefringent crystals.

the *c*-direction and the in-plane direction, which may be the primary origin of birefringence in $Ba_3P_2Se_8$. In contrast, the interlayer gap in $Ba_4HgP_2Se_{10}$ is further expanded due to the incorporation of the [$HgSe_2$] unit, which further decreases the electron density in the *c*-direction. This further enhances the electron density contrast between the *c*-direction and within the layer, contributing to an enhanced birefringence mechanism. Additionally, apart from the contribution from the layered framework, the electron cloud around the [$HgSe_2$] unit in $Ba_4HgP_2Se_{10}$ exhibits significant anisotropy. Gaussian calculations indicate that its polarizability anisotropy is as high as 117.5, which is substantially greater than the anisotropy value of 9.0 of the [PSe_4] unit, suggesting that the [$HgSe_2$] unit also plays a significant role in enhancing birefringence. Furthermore, since all the [$HgSe_2$] units in the structure are arranged in parallel and their projection along the *b*-axis is significantly larger than those in other directions (Fig. 3c), the electron density along the *b*-axis is substantially higher compared to the *a*- and *c*-axes (Fig. 3d and e). This may lead to a significantly stronger response in the *b* direction than those in the *a* and *c* directions when interacting with the incident light, causing the wave velocity in the *b* direction to decrease more significantly than those in the *a* and *c* directions, and thus the refractive index along the *b* direction is significantly higher than those along the *a* and *c* directions, which could be another main reason for the large birefringence of $Ba_4HgP_2Se_{10}$ and is consistent with the calculated refractive index dispersion curves ($n_b > n_a > n_c$) (Fig. S8†). That is, the cooperation of the laminar framework and the linear [$HgSe_2$] unit creates the large birefringence of $Ba_4HgP_2Se_{10}$. Notably, the birefringence of $Ba_4HgP_2Se_{10}$ exceeds those of many commercially available birefringent crystals, such as α-BBO (Δn = 0.116 at 1064 nm),[15] $LiNbO_3$ (Δn = 0.089 at 1064 nm),[12] and MgF_2 (Δn = 0.012 at 1064 nm)[16] (Fig. 4). Moreover, it also possesses a large band gap and a wide IR transmission range. These results indicate that $Ba_4HgP_2Se_{10}$ should be a promising IR birefringent crystal.

Conclusions

In summary, a "low-dimensional motif intercalation" strategy was employed for the successful synthesis of $Ba_4HgP_2Se_{10}$ by introducing linear [$HgSe_2$] units into the layered selenophosphide $Ba_3P_2Se_8$. A promising novel IR birefringent crystal, $Ba_4HgP_2Se_{10}$, was successfully synthesized. $Ba_4HgP_2Se_{10}$ achieves a balance between a wide IR transmission range, large birefringence, and a wide band gap, making it a potential IR birefringent crystal. The bulk crystal growth of $Ba_4HgP_2Se_{10}$ will be performed to accurately determine the refractive indices. This work provides a new synthesis strategy for designing novel IR birefringent crystalline materials.

Data availability

The raw data supporting the conclusions of this manuscript will be made available by the authors. The authors confirm that the data supporting the findings of this study are available within the article.

Conflicts of interest

The authors declare no competing financial interests.

Acknowledgements

This work was supported by the National Natural Science Foundation of China (52172011 and 52402013), the CAS Project for Young Scientists in Basic Research (YSBR-024), the

RCWM/CMA-CUIT (2024GDRY007), and the Natural Science Foundation of Sichuan (2023NSFSC1274).

References

1 A. Tagaya, H. Ohkita, M. Mukoh, R. Sakaguchi and Y. Koike, Compensation of the Birefringence of a Polymer by a Birefringent Crystal, *Science*, 2003, **301**, 812–814.

2 Y. Zhou, Z. F. Guo, H. G. Gu, Y. Q. Li, Y. P. Song, S. Y. Liu, M. C. Hong, S. G. Zhao and J. H. Luo, A solution-processable natural crystal with giant optical anisotropy for efficient manipulation of light polarization, *Nat. Photonics*, 2024, **18**, 922–927.

3 X. Chen, W. G. Lu, J. Tang, Y. Zhang, Y. Wang, G. D. Scholes and H. Zhong, *Nat. Photonics*, 2021, **15**, 813–816.

4 J. Y. Guo, A. Tudi, S. J. Han, Z. H. Yang and S. L. Pan, α-SnF_2: AUV Birefringent Material with Large Birefringence and Easy Crystal Growth, *Angew. Chem., Int. Ed.*, 2021, **60**, 3540–3544.

5 S. Y. Niu, G. Joe, H. Zhao, Y. C. Zhou, T. Orvis, H. X. Huyan, J. Salman, K. Mahalingam, B. Urwin, J. B. Wu, Y. Liu, T. E. Tiwald, S. B. Cronin, B. M. Howe, M. Mecklenburg, R. Haiges, D. J. Singh, H. Wang, M. A. Kats and J. Ravichandran, *Nat. Photonics*, 2018, **12**, 392–396.

6 Y. Q. Li, X. Zhang, J. Y. Zheng, Y. Zhou, W. Q. Huang, Y. P. Song, H. Wang, X. Y. Song, J. H. Luo and S. G. Zhao, A Hydrogen Bonded Supramolecular Framework Birefringent Crystal, *Angew. Chem., Int. Ed.*, 2023, **62**, e202304498.

7 Z. Y. Xie, L. G. Sun, G. Z. Han and Z. Z. Gu, Optical Switching of a Birefringent Photonic Crystal, *Adv. Mater.*, 2008, **20**, 3601–3604.

8 M. R. Sun, H. J. Su, W. H. Liu and J. Y. Yao, $Ba_4Cd_2Ge_2Te_9$: A promising infrared functional crystal with large birefringent and photoluminescence properties, *J. Alloys Compd.*, 2024, **977**, 173348.

9 M. S. Zhang, W. D. Yao, S. M. Pei, B. W. Liu, X. M. Jiang and G. C. Guo, $HgBr_2$: An Easily Growing Wide-Spectrum Birefringent Crystal, *Chem. Sci.*, 2024, **15**, 6891–6896.

10 L. T. Jiang, X. M. Jiang, Y. H. Fan, B. W. Liu and G. C. Guo, Reconstructing nearly isotropic microstructures to construct a one-dimensional framework causing record birefringence in thiophosphates, *Chem. Sci.*, 2024, **15**, 17114.

11 H. T. Luo, T. Tkaczyk, E. L. Dereniak, K. Oka and R. Sampson, High Birefringence of the Yttrium Vanadate Crystal in the Middle Wavelength Infrared, *Opt. Lett.*, 2006, **31**, 616–618.

12 G. D. Boyd, R. C. Miller, K. Nassau, W. L. Bond and A. Savage, $LiNbO_3$: An Efficient Phase Matchable Nonlinear Optical Material, *Appl. Phys. Lett.*, 1964, **5**, 234–236.

13 G. Ghosh, Dispersion-equation coefficients for the refractive index and birefringence of calcite and quartz crystals, *Opt. Commun.*, 1999, **163**, 95–102.

14 J. Rams, A. Tejeda and J. M. Cabrera, Refractive indices of rutile as a function of temperature and wavelength, *J. Appl. Phys.*, 1997, **82**, 994–997.

15 G. Q. Zhou, J. Xu, X. D. Chen, H. Y. Zhong, S. T. Wang, K. Xu, P. Z. Deng and F. X. Gan, Growth and spectrum of a novel birefringent α-BaB_2O_4 crystal, *J. Cryst. Growth*, 1998, **191**, 517–519.

16 M. J. Dodge, Refractive Properties of Magnesium Fluoride, Refractive properties of magnesium fluoride, *Appl. Opt.*, 1984, **23**, 1980–1985.

17 Z. Li, J. Y. Yao and Y. C. Wu, Chalcophosphates: A Treasure House of Infrared Nonlinear Optical Materials, *Cryst. Growth Des.*, 2020, **20**, 7550–7564.

18 X. Zhang, J. Y. Yao, W. L. Yin, Y. Zhu, Y. C. Wu and C. T. Chen, Determination of the nonlinear optical coefficients of the $BaGa_4Se_7$ crystal, *Opt. Express*, 2015, **23**, 552–558.

19 Z. X. Zheng, Z. X. Qiu, C. H. Xie, Y. P. Zhang, X. M. Jiang, B. W. Liu and G. C. Guo, Remarkable phase-matchable second-harmonic generation realized by strong polarities of $[PbSe_3]$ and $[GaSe_4]$ functional motifs in $PbGa_4Se_7$, *Sci. China Mater.*, 2023, **66**, 2795–2802.

20 X. Lin, Y. Guo and N. Ye, $BaGa_2GeX_6$ (X = S, Se): New mid-IR nonlinear optical crystals with large band gaps, *J. Solid State Chem.*, 2012, **195**, 172–177.

21 T. K. Bera, J. I. Jang, J. H. Song, C. D. Malliakas, A. J. Freeman, J. B. Ketterson and M. G. Kanatzidis, Soluble Semiconductors $AAsSe_2$ (A = Li, Na) with a Direct-Band-Gap and Strong Second Harmonic Generation: A Combined Experimental and Theoretical Study, *J. Am. Chem. Soc.*, 2010, **132**, 3484–3495.

22 Y. Guo, F. Liang, W. Yin, Z. Li, X. Luo, Z. S. Lin, J. Yao, A. Mar and Y. Wu, $BaHgGeSe_4$ and $SrHgGeSe_4$: Two New Hg-Based Infrared Nonlinear Optical Materials, *Chem. Mater.*, 2019, **31**, 3034–3040.

23 Z. Z. Luo, C. S. Lin, H. H. Cui, W. L. Zhang, H. Zhang, H. Chen, Z. Z. He and W. D. Cheng, $PbGa_2MSe_6$ (M = Si, Ge): Two Exceptional Infrared Nonlinear Optical Crystals, *Chem. Mater.*, 2015, **27**, 914–922.

24 X. M. Jiang, S. Deng, M. H. Whangbo and G. C. Guo, Material Research from the Viewpoint of Functional Motifs, *Natl. Sci. Rev.*, 2022, **9**, nwac017.

25 C. C. Tu, W. Q. Jin, A. Tudi, C. W. Xie and Z. H. Yang, $CaBO_2F$: A novel deep-UV structural template with high nonlinear optical performance induced by electron delocalization, *Sci. China Mater.*, 2023, **66**, 1197–1204.

26 H. Zhou, M. Cheng, D. D. Chu, X. Liu, R. An, S. L. Pan and Z. H. Yang, Sulfate Derivatives with Heteroleptic Tetrahedra: New Deep Ultraviolet Birefringent Materials in which Weak Interactions Modulate Functional Module Ordering, *Angew. Chem., Int. Ed.*, 2024, **64**, e202413680.

27 B. B. Zhang, G. P. Han, Y. Wang, X. L. Chen, Z. H. Yang and S. L. Pan, Expanding Frontiers of Ultraviolet Nonlinear Optical Materials with Fluorophosphates, *Chem. Mater.*, 2018, **30**, 5397–5403.

28 C. Wang, C. S. Lin, X. Zhao, S. D. Yang, T. Yan, S. H. Fang, L. L. Wu, N. Ye and M. Luo, Design of High-Performance Infrared Nonlinear Optical PAs_3S_3 with Perfectly Aligned Polar Molecular Cage via a Bipolar-Axis-Symmetry Coupling Strategy, *Angew. Chem., Int. Ed.*, 2024, **64**, e202421825.
29 L. L. Cao, H. T. Tian, D. H. Lin, C. S. Lin, F. Xu, Y. L. Han, T. Yan, J. D. Chen, B. X. Li, N. Ye and M. Luo, A flexible functional module to regulate ultraviolet optical nonlinearity for achieving a balance between a second-harmonic generation response and birefringence, *Chem. Sci.*, 2022, **13**, 6990.
30 H. T. Tian, N. Ye and M. Luo, Sulfamide: A Promising Deep-Ultraviolet Nonlinear Optical Crystal Assembled from Polar Covalent $[SO_2(NH_2)_2]$ Tetrahedra, *Angew. Chem., Int. Ed.*, 2022, **61**, e202200395.
31 X. Hao, M. Luo, C. S. Lin, G. Peng, F. Xu and N. Ye, M $(NH_2SO_3)_2$ (M = Sr, Ba): Two Deep-Ultraviolet Transparent Sulfamates Exhibiting Strong Second Harmonic Generation Responses and Moderate Birefringence, *Angew. Chem., Int. Ed.*, 2020, **60**, 7621–7625.
32 G. M. Sheldrick, A short history of SHELX, *Acta Crystallogr.*, 2008, **64**, 112–122.
33 W. Kohn, Nobel Lecture: Electronic structure of matter-wave functions and density functionals, *Rev. Mod. Phys.*, 1999, **71**, 1253–1266.
34 J. P. Perdew, K. Burke and M. Ernzerhof, Generalized Gradient Approximation Made Simple, *Phys. Rev. Lett.*, 1996, **77**, 3865.
35 H. J. Monkhorst and J. D. Pack, Special points for Brillouin-zone integrations, *Phys. Rev. B*, 1976, **13**, 5188–5192.
36 I. Chung, C. D. Malliakas, J. I. Jang, C. G. Canlas, D. P. Weliky and M. G. Kanatzidis, Helical Polymer $1/_\infty[P_2Se_6^{2-}]$: Strong Second Harmonic Generation Response and Phase-Change Properties of Its K and Rb Salts, *J. Am. Chem. Soc.*, 2007, **129**, 14996–15006.
37 S. Banerjee, C. D. Malliakas, J. I. Jang, J. B. Ketterson and M. G. Kanatzidis, $1/_\infty[ZrPSe^{6-}]$: A Soluble Photoluminescent Inorganic Polymer and Strong Second Harmonic Generation Response of Its Alkali Salts, *J. Am. Chem. Soc.*, 2008, **130**, 12270–12272.
38 I. Chung, J. I. Jang, C. D. Malliakas, J. B. Ketterson and M. G. Kanatzidis, Strongly Nonlinear Optical Glass Fibers from Noncentrosymmetric Phase-Change Chalcogenide Materials, *J. Am. Chem. Soc.*, 2010, **132**, 384–389.
39 I. Chung, M. G. Kim, J. I. Jang, J. He, J. B. Ketterson and M. G. Kanatzidis, Strongly Nonlinear Optical Chalcogenide Thin Films of $APSe_6$ (A = K, Rb) from Spin-Coating, *Angew. Chem., Int. Ed.*, 2011, **50**, 10867–10870.
40 A. S. Haynes, F. O. Saouma, C. O. Otieno, D. J. Clark, D. P. Shoemaker, J. I. Jang and M. G. Kanatzidis, Phase-Change Behavior and Nonlinear Optical Second and Third Harmonic Generation of the One-Dimensional $K_{(1-x)}Cs_xPSe_6$ and Metastable β-$CsPSe_6$, *Chem. Mater.*, 2015, **27**, 1837–1846.
41 J. C. Syrigos, D. J. Clark, F. O. Saouma, S. M. Clarke, L. Fang, J. I. Jang and M. G. Kanatzidis, Semiconducting Properties and Phase Matching Nonlinear Optical Response of the One-Dimensional Selenophosphates ANb_2PSe_{10} (A = K, Rb, and Cs), *Chem. Mater.*, 2015, **27**, 255–265.
42 I. Chung, J. H. Song, J. I. Jang, A. J. Freeman, J. B. Ketterson and M. G. Kanatzidis, Flexible Polar Nanowires of $Cs_5BiP_4Se_{12}$ from Weak Interactions between Coordination Complexes: Strong Nonlinear Optical Second Harmonic Generation, *J. Am. Chem. Soc.*, 2009, **131**, 2647–2656.
43 I. Chung, J. I. Jang, M. A. Gave, D. P. Weliky and M. G. Kanatzidis, Low Valent Phosphorus in the Molecular Anions $[P_5Se_{12}]^{5-}$ and β-$[P_6Se_{12}]^{4-}$: Phase Change Behavior and near Infrared Second Harmonic Generation, *Chem. Commun.*, 2007, **47**, 4998–5000.
44 C. D. Morris, I. Chung, S. Park, C. M. Harrison, D. J. Clark, J. I. Jang and M. G. Kanatzidis, Molecular Germanium Selenophosphate Salts: Phase-Change Properties and Strong Second Harmonic Generation, *J. Am. Chem. Soc.*, 2012, **134**, 20733–20744.
45 G. Zhang, L. Wei, L. Zhang, X. Wang, B. Liu, X. Zhao and X. Tao, Growth and polarized Raman spectroscopy investigations of single crystal $CdSiP_2$: Experimental measurements and ab initio calculations, *J. Cryst. Growth*, 2017, **473**, 28–33.
46 G. A. Medvedkin and V. G. Voevodin, Magnetic and optical phenomena in nonlinear optical crystals $ZnGeP_2$ and $CdGeP_2$, *J. Opt. Soc. Am. B*, 2005, **22**, 1884–1898.
47 A. J. Springthorpe and J. G. Harrison, $MgSiP_2$: A New Member of the II-IV-V_2 Family of Semiconducting Compounds, *Nature*, 1969, **222**, 977.
48 G. Ambrazevičius, G. Babonas, Y. V. Rud and A. Šileika, The Fundamental Absorption Edge of $MgSiP_2$, *Phys. Status Solidi B*, 1981, **106**, 85–89.
49 G. C. Catella and D. Burlage, Crystal Growth and Optical Properties of $AgGaS_2$ and $AgGaSe_2$, *MRS Bull.*, 1998, **23**, 28–36.

